International Journal of Minerals, Metallurgy and Materials
Volume 29, Number 2, February 2022, Page 263
https://doi.org/10.1007/s12613-020-2199-5

Effect of cathodic potential on stress corrosion cracking behavior of 21Cr2NiMo steel in simulated seawater

Menghao Liu[1)], *Zhiyong Liu*[1),✉], *Cuiwei Du*[1),✉], *Xiaoqin Zhan*[2)], *Chunduo Dai*[1)], *Yue Pan*[1)], *and Xiaogang Li*[1)]

1) Corrosion and Protection Center, University of Science and Technology Beijing, Beijing 10083, China
2) Zhengmao Group Co., Ltd., Zhenjiang 212000, China
(Received: 22 May 2020; revised: 17 September 2020; accepted: 21 September 2020)

Abstract: This study aims at providing systematically insights to clarify the impact of cathodic polarization on the stress corrosion cracking (SCC) behavior of 21Cr2NiMo steel. Slow-strain-rate tensile tests demonstrated that 21Cr2NiMo steel is highly sensitive to hydrogen embrittlement at strong cathodic polarization. The lowest SCC susceptibility occurred at −775 mV vs. SCE, whereas the SCC susceptibility was remarkably higher at potentials below −950 mV vs. SCE. Scanning electron microscopy (SEM) and electron backscattered diffraction (EBSD) revealed that the cathodic potential decline caused a transition from transgranular to intergranular mode in the fracture path. The intergranular mode transformed from bainite boundaries separation to prior austenitic grain boundaries separation under stronger cathodic polarization. Furthermore, corrosion pits promoted the nucleation of SCC cracks. In conclusion, with the decrease in the applied potential, the SCC mechanism transformed from the combination of hydrogen embrittlement and anodic dissolution to typical hydrogen embrittlement.

Keywords: stress corrosion cracking; cathodic potential; hydrogen embrittlement; seawater; high-strength low-alloy steel

1. Introduction

High-strength low-alloy (HSLA) steel has been extensively adopted to construct off-shore platforms because of its high strength and economic value [1–3]. The 1000 MPa-grade 21Cr2NiMo steel has been widely used for stabilizing offshore platforms. Because of the long-term usage of the platform, the high stress level from external loads, and impressed current fluctuations flowing from the platform, the platform is exposed to stress corrosion cracking (SCC) [4–6]. As the HSLA strength increases, the alloy becomes susceptible to SCC [7–8]. Cases and application profiles of SCC have been reported in the literature [9–12] .

The SCC mechanism of HSLA under marine conditions mainly consists of hydrogen embrittlement and anodic dissolution [13–15]. Moreover, cathodic potentials have been considered a vital variable for SCC [16–19]. Zheng *et al.* [20] reported that cathodic potential can cause the SCC of Welten 60 steel. Zielinskia and Domzalicki [21] observed that applying cathodic polarization makes HSLA 17HMBVA steel partly susceptible to hydrogen embrittlement. Du *et al.* [22] found that anodic dissolution controlled the SCC of A537 steel at anodic potential and that hydrogen-induced cracking dominated at high cathodic potentials. Ma *et al.* [23] discovered that the susceptibility of E690 steel drastically increased when the cathodic polarization potential was less than −950 mV vs. SCE.

In this study, electrochemical tests combined with slow-strain-rate testing (SSRT) measurements were conducted on 21Cr2NiMo steel in simulated water to investigate how cathodic potential influences the SCC behavior. This work will provide an experimental basis for the safe service of the mooring chain steel.

2. Experimental

2.1. Materials

The test material in this study was 21Cr2NiMo steel acquired from Zhenjiang Anchorage Chain Factory (China). The steel contains (in weight percent) 0.23% C, 0.23% Si, 0.59% Mn, 1.91% Cr, 0.91% Ni, 0.44% Mo, and Fe balance. The yield strength and the ultimate tensile strength of the steel were 939 and 1047 MPa, respectively. The toughness of the material included a Charpy energy of 155 J, an area reduction of 58.88%, and a length elongation of 15.84% at room temperature. As shown in Fig. 1, the steel matrix was lath bainite. The inverse pole figure map revealed no distinct texture in the steel (Fig. 2). The grain boundaries map showed that the bainitic grain boundaries and the prior austenite boundaries were high-angle boundaries, which is a distinct characteristic of lath bainite [24]. The average equivalent circle diameter of grains was about 2 μm. The test

✉ Corresponding authors: Cuiwei Du E-mail: dcw@ustb.edu.cn; Zhiyong Liu E-mail: liuzhiyong7804@ustb.edu.cn

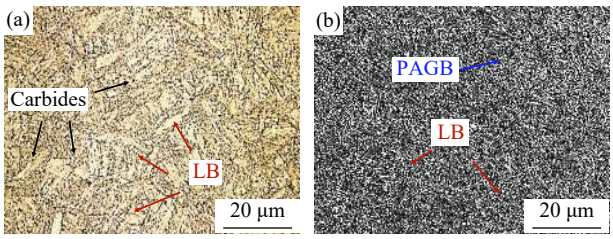

Fig. 1. Microstructure of 21Cr2NiMo steel: (a) metallographic image; (b) scanning electron microscopy image. The blue arrow represents prior austenitic grain boundaries (PAGB), the pink arrows represent bainitic lath boundaries (LB), and the black arrows represent spherical carbides scattered along the grain boundaries.

solution was prepared according to ASTM D1141–98, with the following composition (g/L): 24.53 NaCl, 4.09 Na_2SO_4, 11.11 $MgCl_2{\cdot}6H_2O$, 1.14 $CaCl_2$, 0.042 $SrCl_2{\cdot}6H_2O$, 0.70 KCl, 0.20 $NaHCO_3$, 0.10 KBr, 0.027 H_2BO_3, and 0.003 NaF. After the ingredients were dissolved in deionized water, the pH value was adjusted to 8.2 with 0.1 mol/L NaOH solution.

2.2. SSRT tests

Slow-strain rate tensile measurements were conducted at a speed of 1.0×10^{-6} s^{-1} using the traditional three-electrode system. The size of the flat-plate tensile specimen is displayed in Fig. 3. The tensile sample was polished by successive silicon carbide papers from 400# to 2000# with the last polishing scratches parallel to the length direction. Then, it was ultrasonically cleaned by deionized water. Afterward, silicone gel was used to seal the specimen, with 25 mm exposed length as the working area.

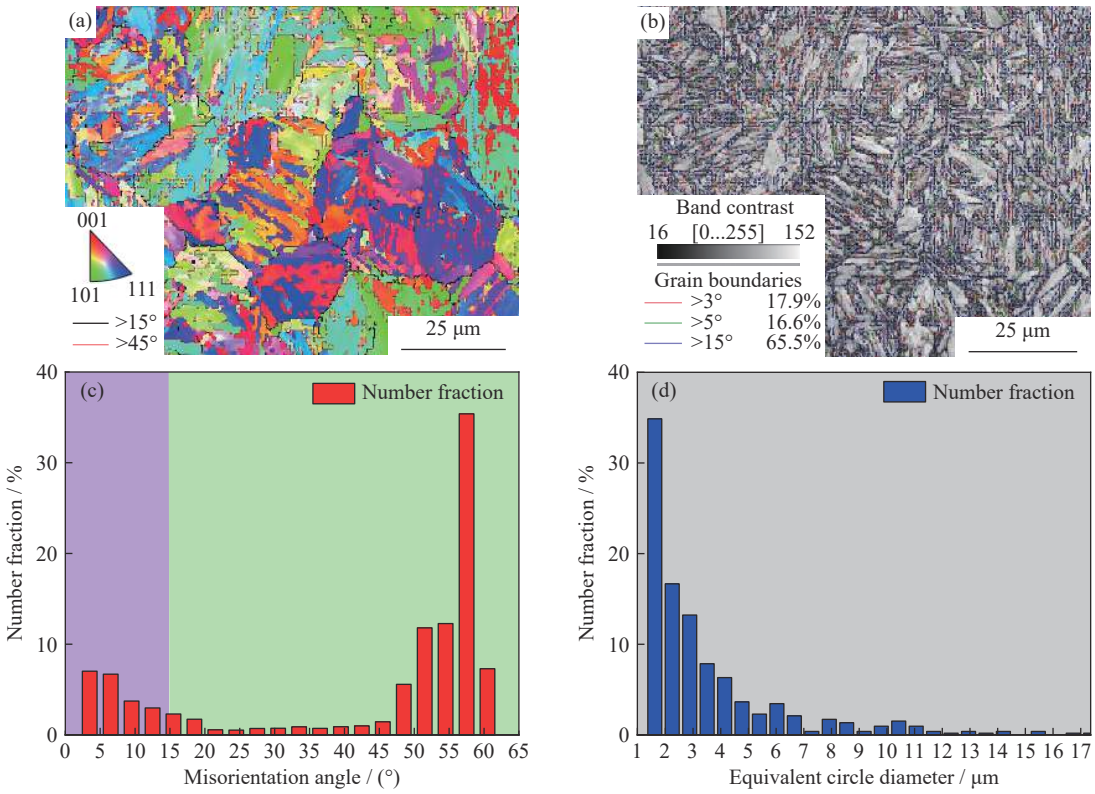

Fig. 2. (a) Inverse pole figure; (b) the corresponding grain boundary map; (c) the corresponding misorientation angle distribution; (d) the corresponding equivalent circle diameter distribution. Green and blue lines represent high-angle grain boundaries with tolerance angles of <45° and >45°, respectively, and red lines represent low-angle boundaries with a tolerance angle of <15°.

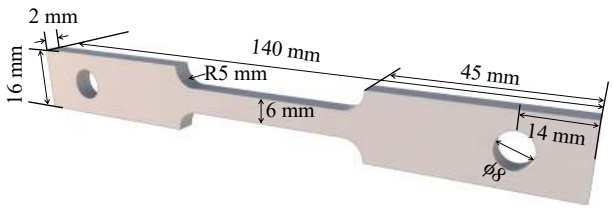

Fig. 3. Dimensions of specimen for SSRT.

Prior to each measurement, a 1000 N force was applied to the specimen for 24 h to avoid the gap and stabilize the stress state between the SSRT machine and the specimen. After fracture occurred, corrosion deposits were removed in a descaling solution with 500 mL deionized water, 500 mL 38wt% hydrochloric acid, and 3.5 g hexamethylenetetramine. Fracture morphologies were observed and measured via scanning electron microscopy (SEM) and electron backscattered diffraction (EBSD). Then, the loss in area reduction (I_Ψ) and the loss in elongation (I_δ) were measured relative to the data in air. The formulas are as follows:

$$I_\Psi = (\Psi_0 - \Psi_s)/\Psi_0 \times 100\% \quad (1)$$

$$I_\delta = (\delta_0 - \delta_s)/\delta_0 \times 100\% \quad (2)$$

where Ψ_s and Ψ_0 are the area reductions of the SSRT samples in simulated seawater and air, respectively, and δ_s and δ_0 are the elongations of SSRT samples in simulated seawater and

air, respectively.

2.3. Electrochemical measurements

The electrochemical working station (Versa STAT 3F) used in this study operated with a traditional three-electrode system. A platinum sheet (20 mm × 20 mm), a saturated calomel electrode (SCE), and the test steel were the counter electrode, reference electrode, and working electrode, respectively. The working area was 1 cm^2, which was sealed with epoxy resin. Before electrochemical tests, the open-circuit potential (OCP) was tested for 1600 s to ensure stability. The scanning rates of potentiodynamic polarization tests were 0.3 and 30 mV/s from −1200 to −200 mV vs. SCE. The above scanning speeds were chosen because they can represent the electrochemical states at different positions on the crack. A previous study has also proved its availability [23]. Each measurement was conducted at least three times.

3. Results

3.1. SSRT test

Fig. 4 depicts the stress–strain curves obtained from the SSRT tests. The plastic zones differed, whereas the elastic zones coincided with one another. In general, the strength changed only slightly with the cathodic potential (Fig. 5); however, it grew dramatically when the cathodic potential was below −900 mV vs. SCE, and the yield strength at −1200 mV vs. SCE was even higher than that in air. This was because the slipping of dislocations was restrained by permeated hydrogen atoms, which generate from the electrochemical reaction during the corrosion process [25–27].

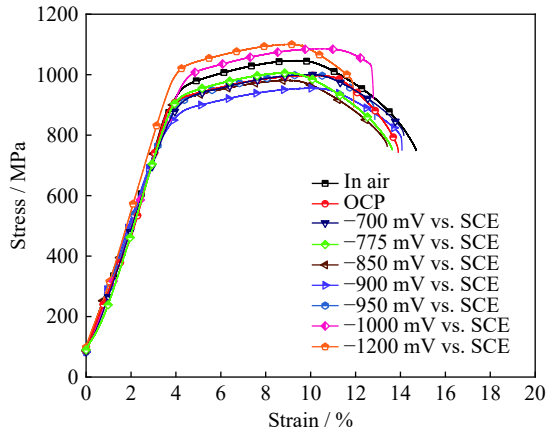

Fig. 4. Stress–strain curves obtained from the SSRT tests under successive potentials in simulated seawater.

Moreover, both the elongation and strength under the other conditions were lower than those in air. The SCC sensitivity calculated based on the length elongation and area reduction of test specimens is illustrated as Fig. 6. The loss proportion of elongation reduction was about 10%, from −700 to −900 mV vs. SCE, and then it increased to about 30%. The loss proportion of area reduction was below 10% at OCP, indicating that 21Cr2NiMo presented no significant SCC susceptibility at OCP. The loss proportion reached the lowest

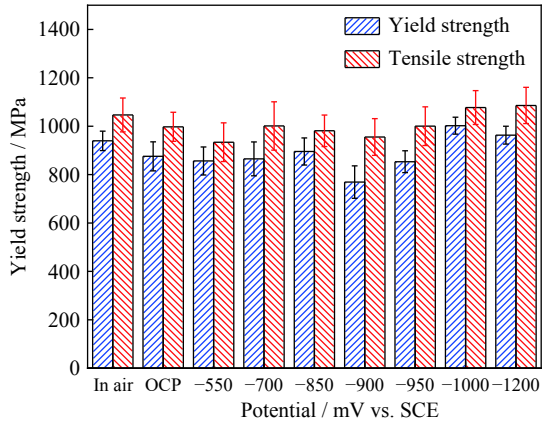

Fig. 5. Yield strength and tensile strength of 21Cr2NiMo at different potentials in simulated seawater.

value at −775 mV vs. SCE, increased slowly from −775 to −900 mV vs. SCE and then rapidly after −950 mV vs. SCE, and was highest (~50%) at −1200 mV vs. SCE. Thus, the SCC behavior of the 21Cr2NiMo steel rapidly deteriorated when the hydrogen evolution reaction was enhanced [28–31].

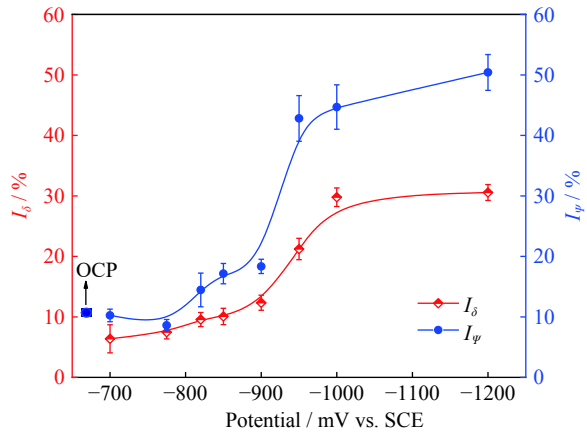

Fig. 6. SCC susceptibility of 21Cr2NiMo obtained at a strain rate of 1.0 × 10^{-6} s^{-1} in simulated seawater at different cathodic potentials.

3.2. Fracture morphologies

Fig. 7 displays the typical fracture and the profile morphologies of the specimens under different conditions. The macromorphology exhibited an apparent necking above −900 mV vs. SCE and an invisible neckdown below −950 mV vs. SCE. The micromorphology in air featured dimples and torn edges. The dimples varied in size because they were nucleated with carbides of different sizes. Mixed zones were observed beyond −900 mV vs. SCE, combined with dimples and flat zones decorated with boundaries separation and secondary cracks. When the cathodic potential shifted negatively from −900 to −1200 mV vs. SCE, the micromorphology showed distinct intergranular fracture, with microcracks along the prior austenitic grain boundaries (Fig. 6) [32–33], indicating a high susceptibility to SCC.

The high-magnification image in Fig. 8 confirms the separation of lath bainite boundaries and short secondary cracks along bainite laths at −850 mV vs. SCE. However, only prior

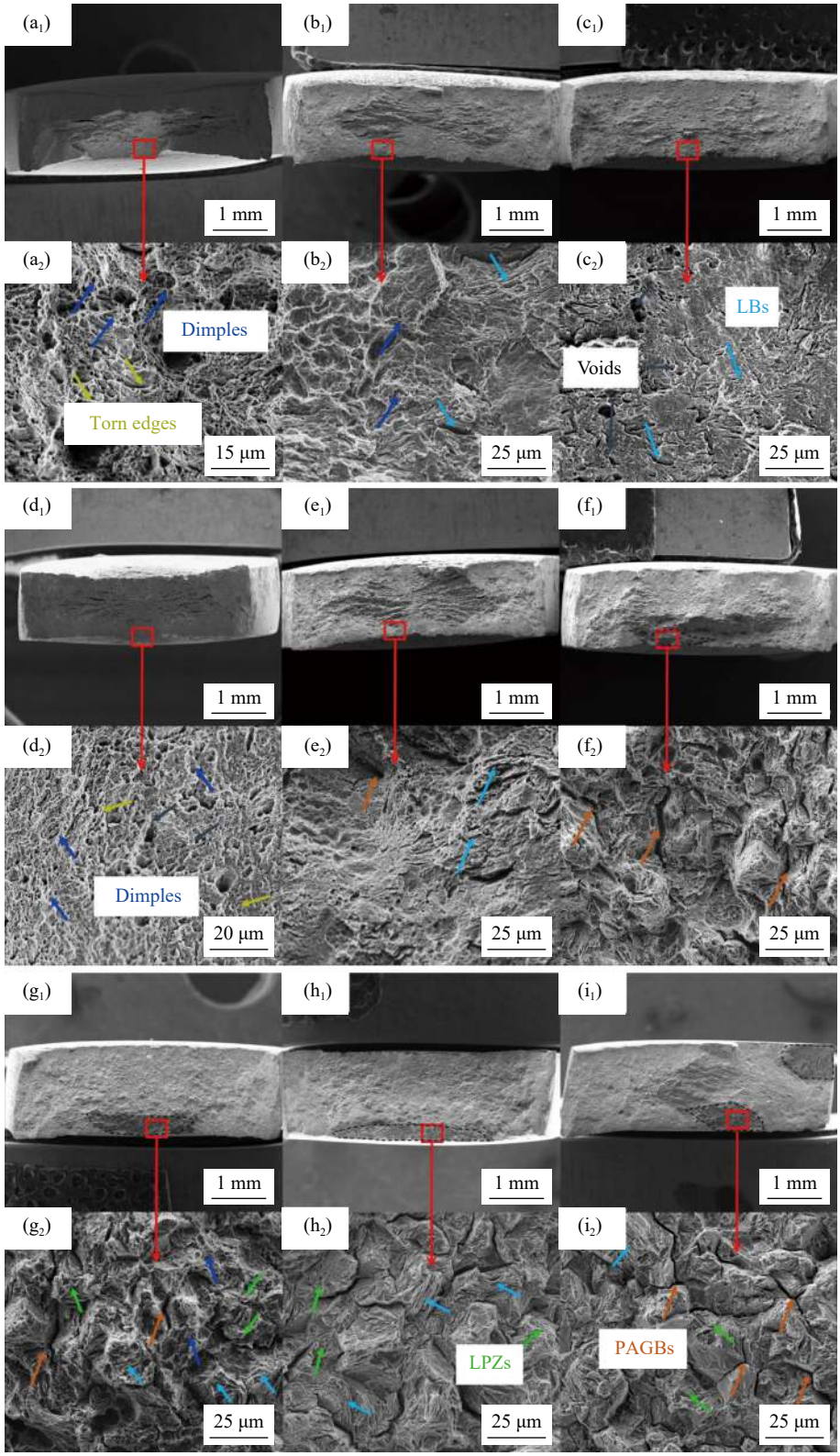

Fig. 7. SEM morphologies of fracture surface in air and at various potentials: (a_1, a_2) in air; (b_1, b_2) OCP; (c_1, c_2) −700 mV vs. SCE; (d_1, d_2) −775 mV vs. SCE; (e_1, e_2) −850 mV vs. SCE; (f_1, f_2) −900 mV vs. SCE; (g_1, g_2) −950 mV vs. SCE; (h_1, h_2) −1000 mV vs. SCE; (i_1, i_2) −1200 mV vs. SCE. Deep blue arrows represent dimple; wathet blue arrows represent lath bainitic boundaries; yellow arrows represent torn edges; orange arrows represent prior austenitic grain boundaries; bright green arrows represent local plastic zones (LPZs).

austenitic grain boundaries separation was observed at −1200 mV vs. SCE, and long secondary cracks distributed at the trigeminal grain boundary of prior austenite. The change in the separation mode is later discussed.

Fig. 9 displays the typical side morphologies under different conditions. The density of secondary cracks could qualitatively reflect the SCC susceptibility of steels. The secondary cracks density was strongly correlated with the applied

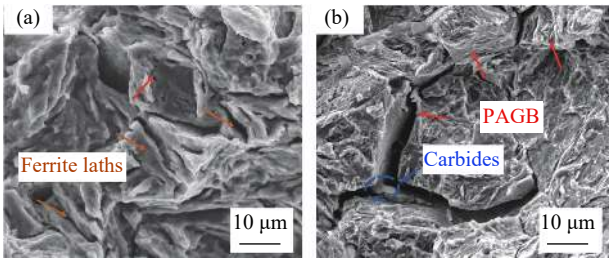

Fig. 8. High-magnification image of fracture morphologies at (a) −850 mV vs. SCE and (b) −1200 mV vs. SCE. Red arrows represent prior austenitic grain boundaries, and pink arrows represent the lath bainite boundaries. Blue arrows represent carbides along prior austenitic grain boundaries.

potential. The side face of the specimen in air and at −775 mV vs. SCE had few side cracks, whereas the secondary crack density increased at potentials below −850 mV vs. SCE. Therefore, the SCC susceptibility increased at strong polarization. Moreover, a long crack resulting from the interconnections of small cracks was observed beyond −1000 mV vs. SCE, whereas only short and sharp cracks appeared when the cathodic potential was below −1000 mV vs. SCE.

Furthermore, crack nucleation from corrosion pits was observed (Fig. 10). At −850 mV vs. SCE, a microcrack initiated at the bottom of corrosion pits, and distinct anodic dissolution could also be observed. This implies that anodic dissolution could exist at typical sites such as the bottom of corrosion pits and crack tips at weak cathodic polarization. Liu *et al.* [34–35] has also proved that anodic dissolution could occur at weak cathodic polarization. In the current study, at −1000 mV vs. SCE, a microcrack initiated from the bottom of corrosion pits and was arrested due to plastic deformation. No further anodic dissolution was observed. Thus, anodic dissolution was fully inhibited at strong cathodic polarization.

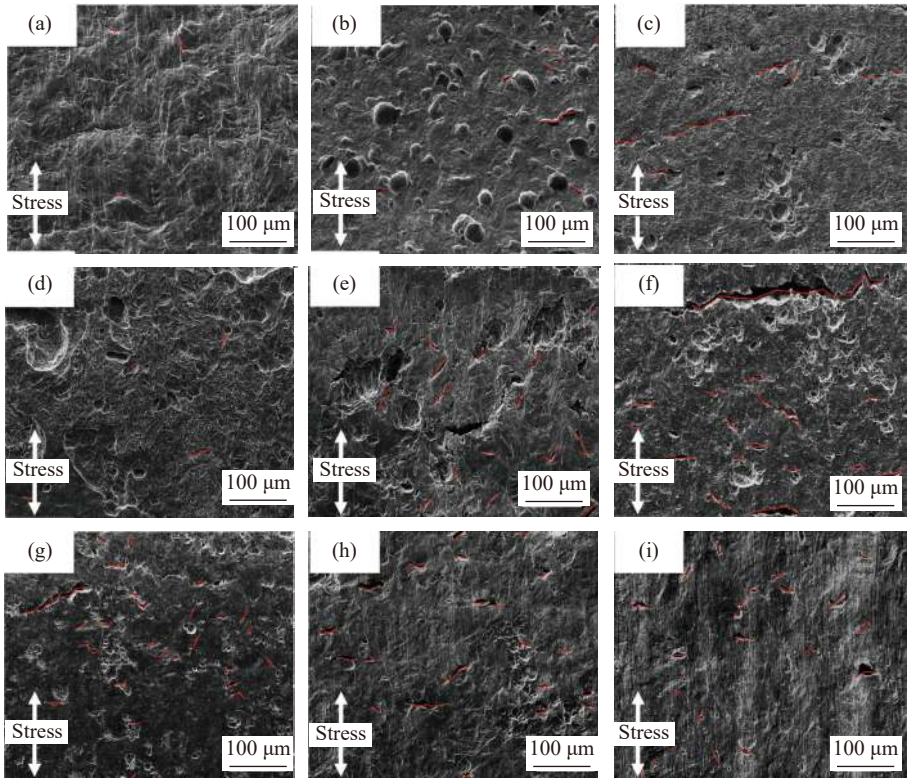

Fig. 9. Morphology of side cracks under different conditions: (a) in air; (b) OCP; (c) −700 mV vs. SCE; (d) −775 mV vs. SCE; (e) −850 mV vs. SCE; (f) −900 mV vs. SCE; (g) −950 mV vs. SCE; (h) −1000 mV vs. SCE; (i) −1200 mV vs. SCE. Secondary cracks longer than 10 μm cracks were indicated by red lines.

Electron backscattered diffraction was conducted to study the propagation mode of cracks, and the results are shown in Fig. 11. At OCP, the crack tip was blunt and the grains near the crack were clearly deformed. The band contrast map revealed that the crack propagated transgranularly. When −700 mV vs. SCE polarization was applied, the crack tip became sharper. This may be because the anodic dissolution in the crack tip was partially inhibited. The crack propagated both intergranularly and transgranularly, and the grain deformation ahead of the crack tip reduced. At −1200 mV vs. SCE, the crack propagated along the high-angle grain boundaries, and no significant grain deformation was observed. The crack tip was sharp and furcated, indicating a small resistance to crack propagation. The cause of the change in crack-

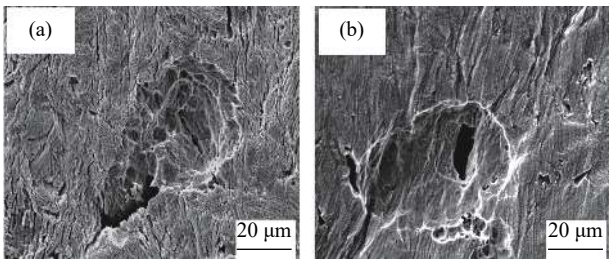

Fig. 10. Secondary cracks initiated from corrosion pits at (a) −850 mV vs. SCE and (b) −1000 mV vs. SCE.

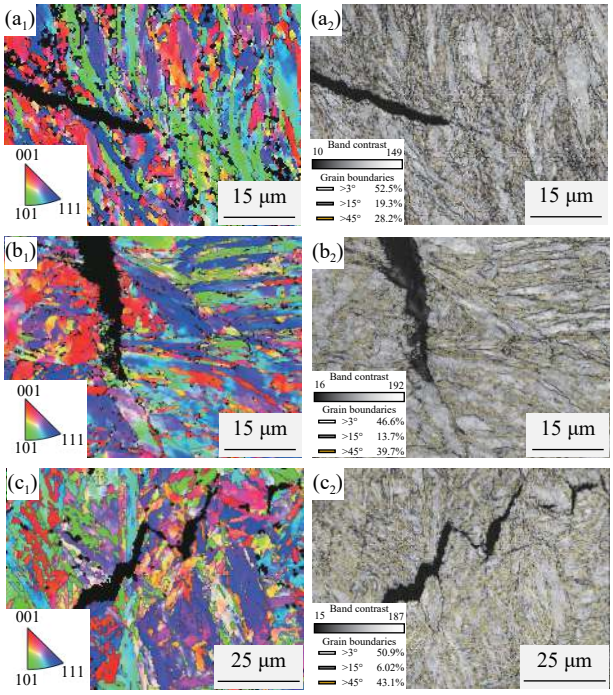

Fig. 11. Inverse pole figure map and band contrast map of secondary cracks at (a_1, a_2) OCP, (b_1, b_2) −700 mV vs. SCE, and (c_1, c_2) −1200 mV vs. SCE.

ing mode may be the hydrogen content exceeding a critical level [19,36]. Grain boundaries have high hydrogen trap binding energy, and hydrogen atoms can easily accumulate at the boundaries. At strong cathodic polarization, the accumulated hydrogen concentration is beyond the critical limit; therefore, the boundaries become the preferential fracture paths.

3.3. Electrochemical property

Fig. 12(a) shows that the OCP of the test steel was −695 mV vs. SCE. Thus, the use of an applied potential of less than −695 mV vs. SCE in the SSRT was of practical significance. Fig. 12(b) displays the polarization curves of test steels at different sweeping rates: 0.3 and 30 mV/s. The polarization curve remarkably changed with the increase in the sweeping rate. When the sweeping rate was 0.3 mV/s, the cathodic branch exhibited a limiting current density, which was controlled by the oxygen diffusion process. With the increase in the sweeping rate to 30 mV/s, the corrosion potential shifted negatively. The current density at 30 mV/s was significantly higher than that at 0.3 mV/s when the applied potential was between −695 and −919 mV vs. SCE, while the cathodic branches were almost overlapped when the applied potential was below −919 mV vs. SCE.

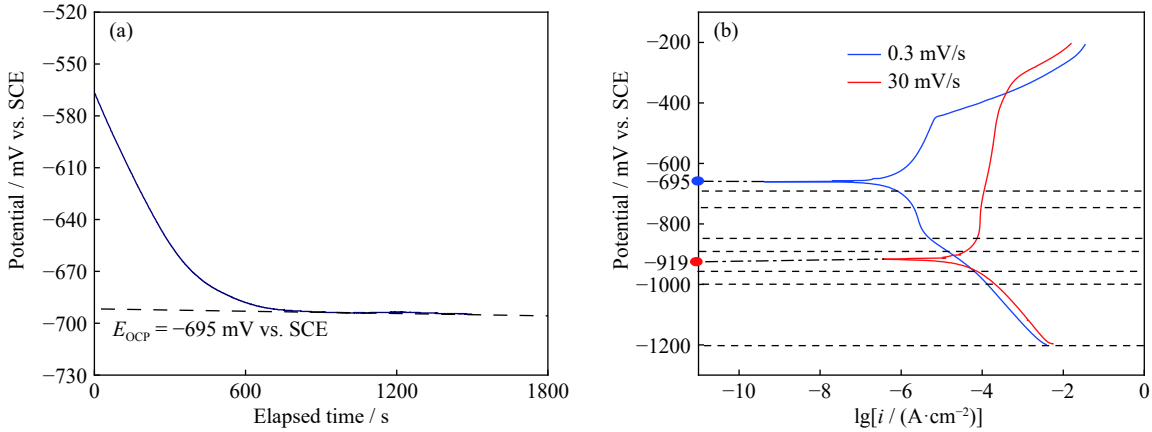

Fig. 12. Electrochemical curves of 21Cr2NiMo in simulated seawater: (a) OCP curves and (b) potentiodynamic curves at 0.3 and 30 mV/s.

4. Discussion

According to Parkins [37] and Liu *et al.* [38], the fast-scan-rate potentiodynamic curve can indicate the electrochemical behavior of fresh metal, as it is too fast for rust to cover the metal under this scanning rate, and the slow-scan-rate curve can indicate the electrochemical behavior of steel covered with corrosion deposits. Moreover, the crack tip is always fresh, whereas the crack wall is always covered with corrosion products; hence, the fast-scan-rate potentiodynamic curve can predict the behavior of the crack tips, and the slow scanning-rate curve can indicate the crack wall behavior. Fig. 12 shows that the 21Cr2NiMo steel underwent anodic dissolution in simulated seawater, as the anodic branches at both 0.3 and 30 mV/s were activation-controlled. Under strong polarization, hydrogen evolution reaction will dominate the cathodic reaction. Hydrogen atoms permeated into the matrix can affect the cracking process [39]. Thus, the SCC of 21Cr2NiMo steel is affected by both hydrogen embrittlement and anodic dissolution. Therefore, the reduction in the loss of area shrinkage at −775 mV vs. SCE was due to the inhibition of iron dissolution, while the increase in the loss of area shrinkage under strong cathodic polarization was due to hydrogen evolution reaction (Fig. 6).

To more comprehensively study the SCC behavior and mechanism of 21Cr2NiMo steel, the applied potentials in Fig. 5 are tagged in Fig. 12, and the applied potential is shown to match different regions in the fast and slow sweeping curves. When the 21Cr2NiMo steel was under potentials of −700, −775, −850, and −900 mV vs. SCE, it was polar-

ized in the anodic state at fast scanning rates and in the cathodic state at slow scanning rates. This means that iron dissolution at the crack tips and hydrogen evolution reaction within the crack wall possibly existed simultaneously; thus, a combination of hydrogen embrittlement and anodic dissolution constituted the SCC mechanism. When the specimen was polarized at −950, −1000, and −1200 mV vs. SCE, the steel was polarized in the cathodic state for both the fast- and slow-scan curves, indicating that hydrogen evolution reaction was dominant at both the crack tip and the crack side regions.

Under different applied potentials, the physical and chemical properties of the crack tip and crack wall differed dramatically. Considering the SSRT results, it can be concluded that at slightly cathodic polarization, such as −775 mV vs. SCE, the crack tip was under anodic dissolution, and the crack wall was polarized in the cathodic state. Hydrogen evolution can occur at the crack tip owing to the blocking effect. Thus, hydrogen atoms can permeate and interact with defects in the steel to promote SCC [34]. The fracture exhibited some brittle regions. Because the critical hydrogen concentration of bainitic grain boundaries was lower than that of the prior austenitic grain boundaries and the hydrogen trap sites of lath boundaries were higher than those of prior austenitic grain boundaries, lath bainite boundaries separated preferentially [40]. The bainitic grain boundaries separation is shown in Fig. 8. When the steel was polarized below −1000 mV vs. SCE, hydrogen evolution reaction dominated both the crack tip and the crack wall. A larger quantity of hydrogen atoms was generated at the crack regions. The fracture shows intergranular morphologies, and the SCC mechanism was completely controlled by hydrogen embrittlement. Moreover, because the hydrogen concentration exceeded the critical concentration of prior austenitic grain boundaries and the cohesive strength of prior austenitic grain boundaries was lower than that of bainitic lath boundaries, the prior austenitic grain boundaries separated preferentially [41].

5. Conclusions

(1) In this study, 21Cr2NiMo steel presented high SCC susceptibility at high cathodic potentials. The SCC susceptibility was lowest at a potential of −775 mV vs. SCE and was remarkably higher at cathodic potentials below −950 mV vs. SCE.

(2) When the cathodic potential was below −950 mV vs. SCE, the SCC mechanism was typical hydrogen embrittlement. When the cathodic potential was between −700 mV vs. SCE and −900 mV vs. SCE, the SCC mechanism was a combination of hydrogen embrittlement and anodic dissolution.

(3) The cathodic potential decline induced a transition from transgranular to intergranular mode in the fracture path. The intergranular mode transformed from bainite boundaries separation to prior austenitic grain boundaries separation. Corrosion pits promoted the nucleation of SCC cracks.

Acknowledgement

This work was financially supported by the National Science and Technology Major Project, China (No. 2017-Ⅶ-0012-0109).

Conflict of Interest

The authors declare no potential conflict of interest.

References

[1] P.R. Thies, L. Johanning, I. Bashir, T. Tuk, M. Tuk, M. Marta, and S. Müller-Schütze, Accelerated reliability testing of articulated cable bend restrictor for offshore wind applications, *Int. J. Mar. Energy*, 16(2016), p. 65.

[2] P. Mabelly, P. Bourges, and G. Pont, Effect of metallurgical transformations on weld residual stresses—Application to E690 steel grade, *Mar. Struct.*, 14(2001), No. 4-5, p. 553.

[3] M.H. Mohd and J.K. Paik, Investigation of the corrosion progress characteristics of offshore subsea oil well tubes, *Corros. Sci.*, 67(2013), p. 130.

[4] M. Sun, K. Xiao, C.F. Dong, X.G. Li, and P. Zhong, Effect of stress on electrochemical characteristics of pre-cracked ultrahigh strength stainless steel in acid sodium sulphate solution, *Corros. Sci.*, 89(2014), p. 137.

[5] J. Ćwiek, Hydrogen assisted cracking of high-strength weldable steels in sea-water, *J. Mater. Process. Technol.*, 164-165(2005), p. 1007.

[6] H. Alawi, A. Ragab, and M. Shaban, Stress corrosion cracking of some steels in various environments, *Eng. Fract. Mech.*, 32(1989), No. 1, p. 29.

[7] N.R. Raykar, R.K. Singh Raman, S.K. Maiti, and L. Choudhary, Investigation of hydrogen assisted cracking of a high strength steel using circumferentially notched tensile test, *Mater. Sci. Eng. A*, 547(2012), p. 86.

[8] J.H. Bulloch, Some effects of yield strength on the stress corrosion cracking behaviour of low alloy steels in aqueous environments at ambient temperatures, *Eng. Fail. Anal.*, 11(2004), No. 6, p. 843.

[9] M.Q. Zhang, M. Beer, S.T. Quek, and Y.S. Choo, Comparison of uncertainty models in reliability analysis of offshore structures under marine corrosion, *Struct. Saf.*, 32(2010), No. 6, p. 425.

[10] Y.L. Zhou, J. Chen, and Z.Y. Liu, Corrosion behavior of rusted 550 MPa grade offshore platform steel, *J. Iron Steel Res. Int.*, 20(2013), No. 3, p. 66.

[11] DNV GL, Offshore standard DNV-OS-E302: *Offshore Mooring Chain*, DNV GL, Oslo, 2018.

[12] G. Artola, A. Arredondo, A. Fernández-Calvo, and J. Aldazabal, Hydrogen embrittlement susceptibility of R4 and R5 high-strength mooring steels in cold and warm seawater, *Metals*, 8(2018), No. 9, art. No. 700.

[13] W.K. Hao, Z.Y. Liu, W. Wu, X.G. Li, C.W. Du, and D.W. Zhang, Electrochemical characterization and stress corrosion cracking of E690 high strength steel in wet-dry cyclic marine environments, *Mater. Sci. Eng. A*, 710(2018), p. 318.

[14] H.Y. Tian, X. Wang, Z.Y. Cui, Q.K. Lu, L.W. Wang, L. Lei, Y. Li, and D.W. Zhang, Electrochemical corrosion, hydrogen permeation and stress corrosion cracking behavior of E690 steel in thiosulfate-containing artificial seawater, *Corros. Sci.*, 144(2018), p. 145.

[15] Q.K. Lu, L.W. Wang, J.C. Xin, H.Y. Tian, X. Wang, and Z.Y. Cui, Corrosion evolution and stress corrosion cracking of E690

steel for marine construction in artificial seawater under potentiostatic anodic polarization, *Constr. Build. Mater.*, 238(2020), art. No. 117763.
[16] C.F. Dong, Z.Y. Liu, X.G. Li, and Y.F. Cheng, Effects of hydrogen-charging on the susceptibility of X100 pipeline steel to hydrogen-induced cracking, *Int. J. Hydrogen Energy*, 34(2009), No. 24, p. 9879.
[17] S.J. Kim, S.K. Jang, and J.I. Kim, Electrochemical study of hydrogen embrittlement and optimum cathodic protection potential of welded high strength steel, *Met. Mater. Int.*, 11(2005), No. 1, p. 63.
[18] C. Batt, J. Dodson, and M.J. Robinson, Hydrogen embrittlement of cathodically protected high strength steel in sea water and seabed sediment, *Br. Corros. J.*, 37(2002), No. 3, p. 194.
[19] H.Y. Tian, J.C. Xin, Y. Li, X. Wang, and Z.Y. Cui, Combined effect of cathodic potential and sulfur species on calcareous deposition, hydrogen permeation, and hydrogen embrittlement of a low carbon bainite steel in artificial seawater, *Corros. Sci.*, 158(2019), art. No. 108089.
[20] W. Zheng, X. Zhu, and L. Su, Effect of cathodic protection on fracture behavior of low-alloy steels in seawater, *Acta Metall. Sinca*, 2(1989), No. 1, p. 57.
[21] A. Zielinski and P. Domzalicki, Hydrogen degradation of high-strength low-alloyed steels, *J. Mater. Process. Technol.*, 133(2003), No. 1-2, p. 230.
[22] X.S. Du, Y.J. Su, J.X. Li, L.J. Qiao, and W.Y. Chu, Stress corrosion cracking of A537 steel in simulated marine environments, *Corros. Sci.*, 65(2012), p. 278.
[23] H.C. Ma, Z.Y. Liu, C.W. Du, H.R. Wang, C.Y. Li, and X.G. Li, Effect of cathodic potentials on the SCC behavior of E690 steel in simulated seawater, *Mater. Sci. Eng. A*, 642(2015), p. 22.
[24] J.S. Kang, J.B. Seol, and C.G. Park, Three-dimensional characterization of bainitic microstructures in low-carbon high-strength low-alloy steel studied by electron backscatter diffraction, *Mater. Charact.*, 79(2013), p. 110.
[25] D. Delafosse and T. Magnin, Hydrogen induced plasticity in stress corrosion cracking of engineering systems, *Eng. Fract. Mech.*, 68(2001), No. 6, p. 693.
[26] Z.Y. Cui, Z.Y. Liu, L.W. Wang, X.G. Li, C.W. Du, and X. Wang, Effect of plastic deformation on the electrochemical and stress corrosion cracking behavior of X70 steel in near-neutral pH environment, *Mater. Sci. Eng. A*, 677(2016), p. 259.
[27] G.A. Zhang and Y.F. Cheng, Micro-electrochemical characterization of corrosion of welded X70 pipeline steel in near-neutral pH solution, *Corros. Sci.*, 51(2009), No. 8, p. 1714.
[28] R.O. Ritchie, M.H.C. Cedeno, V.F. Zackay, and E.R. Parker, Effects of silicon additions and retained austenite on stress corrosion cracking in ultrahigh strength steels, *Metall. Trans. A*, 9(1978), No. 1, p. 35.
[29] C.S. Carter, Fracture toughness and stress corrosion characteristics of a high strength maraging steel, *Metall. Trans.*, 2(1971), No. 6, p. 1621.
[30] S.K. Banerji, C.J. McMahon, and H.C. Feng, Intergranular fracture in 4340-type steels: Effects of impurities and hydrogen, *Metall. Trans. A*, 9(1978), No. 2, p. 237.
[31] Y. Lee and R.P. Gangloff, Measurement and modeling of hydrogen environment-assisted cracking of ultra-high-strength steel, *Metall. Mater. Trans. A*, 38(2007), No. 13, p. 2174.
[32] H. Luo, C.F. Dong, Z.Y. Liu, M.T.J. Maha, and X.G. Li, Characterization of hydrogen charging of 2205 duplex stainless steel and its correlation with hydrogen-induced cracking, *Mater. Corros.*, 64(2013), No. 1, p. 26.
[33] J.L. Cabezas-Villa, J. Lemus-Ruiz, D. Bouvard, O. Jiménez, H.J. Vergara-Hernández, and L. Olmos, Sintering study of Ti6Al4V powders with different particle sizes and their mechanical properties, *Int. J. Miner. Metall. Mater.*, 25(2018), No. 12, p. 1389.
[34] Z.Y. Liu, L. Lu, Y.Z. Huang, C.W. Du, and X.G. Li, Mechanistic aspect of non-steady electrochemical characteristic during stress corrosion cracking of an X70 pipeline steel in simulated underground water, *Corrosion*, 70(2014), No. 7, p. 678.
[35] Z.Y. Liu, X.G. Li, and Y.F. Cheng, Mechanistic aspect of near-neutral pH stress corrosion cracking of pipelines under cathodic polarization, *Corros. Sci.*, 55(2012), p. 54.
[36] S. Bechtle, M. Kumar, B.P. Somerday, M.E. Launey, and R.O. Ritchie, Grain-boundary engineering markedly reduces susceptibility to intergranular hydrogen embrittlement in metallic materials, *Acta Mater.*, 57(2009), No. 14, p. 4148.
[37] R.N. Parkins, Predictive approaches to stress corrosion cracking failure, *Corros. Sci.*, 20(1980), No. 2, p. 147.
[38] Z.Y. Liu, X.G. Li, C.W. Du, G.L. Zhai, and Y.F. Cheng, Stress corrosion cracking behavior of X70 pipe steel in an acidic soil environment, *Corros. Sci.*, 50(2008), No. 8, p. 2251.
[39] S.S. Kasana and O.P. Pandey, Effect of electroslag remelting and homogenization on hydrogen flaking in AMS-4340 ultra-high-strength steels, *Int. J. Miner. Metall. Mater.*, 26(2019), No. 5, p. 611.
[40] P.P. Bai, J. Zhou, B.W. Luo, S.Q. Zheng, P.Y. Wang, and Y. Tian, Hydrogen embrittlement of X80 pipeline steel in H_2S environment: Effect of hydrogen charging time, hydrogen-trapped state and hydrogen charging-releasing-recharging cycles, *Int. J. Miner. Metall. Mater.*, 27(2020), No. 1, p. 63.
[41] R. Matsumoto, M. Riku, S. Taketomi, and N. Miyazaki, Hydrogen–grain boundary interaction in Fe, Fe–C, and Fe–N systems, *Prog. Nucl. Sci. Technol.*, 2(2011), p. 9.